

ARTICLE OPEN



An emerging Asian aerosol dipole pattern reshapes the Asian summer monsoon and exacerbates northern hemisphere warming

Baoqiang Xiang ^{1,2}✉, Shang-Ping Xie ³, Sarah M. Kang ^{4,5} and Ryan J. Kramer ^{6,7}

Since the early 2010s, anthropogenic aerosols have started decreasing in East Asia (EA) while have continued to increase in South Asia (SA). Yet the climate impacts of this Asian aerosol dipole (AAD) pattern remain largely unknown. Using a state-of-the-art climate model, we demonstrate that the climate response is distinctly different between the SA aerosol increases and EA aerosol decreases. The SA aerosol increases lead to ~2.7 times stronger land summer precipitation change within the forced regions than the EA aerosol decreases. Contrastingly, the SA aerosol increases, within the tropical monsoon regime, produce weak and tropically confined responses, while the EA aerosol decreases yield a pronounced northern hemisphere warming aided by extratropical mean westerly and positive air-sea feedbacks over the western North Pacific. By scaling the observed instantaneous shortwave radiative forcing, we reveal that the recent AAD induces a pronounced northern hemisphere extratropical (beyond 30°N) warming ($0.024 \pm 0.010 \text{ }^{\circ}\text{C decade}^{-1}$), particularly over Europe ($0.049 \pm 0.009 \text{ }^{\circ}\text{C decade}^{-1}$). These findings highlight the importance of the pattern effect of forcings in driving global climate and have important implications for decadal prediction.

npj Climate and Atmospheric Science (2023)6:77; <https://doi.org/10.1038/s41612-023-00400-8>

INTRODUCTION

Anthropogenic aerosols (AAs) are a public health concern as air pollution, and a major driver of regional and global climate change via altering cloud properties and radiative forcing^{1–5}. Various types of AAs have distinct effects on climate, and the net radiative forcing is to a large degree determined by the balance between the scattering and the absorption effects. Accurate simulation and projection of the AA-induced climate remain a thorny and challenging issue, partially due to the inadequate representation of the chemical composition, spatiotemporal variability of different types of AAs, and their complex interactions with clouds^{6–8}.

Along with the economic development and emission policy changes, the geographic pattern of AAs has changed dramatically in the historical period^{9–11}. Since around the 1980s, the major emission sources shifted from the western hemisphere to the eastern hemisphere, characterized by reduced aerosol emissions over North America and Europe but increased aerosol emissions over South Asia (SA) and East Asia (EA). Changes in AAs were suggested to influence both the mean climate and extreme occurrences, such as heavy precipitation intensity and consecutive dry days^{12,13}, extreme fire weather¹⁴, and heat extremes^{15,16}. Particularly, the hemispheric-scale shift of emission sources since around the 1980s was argued to contribute to the observed weakening of the summer Eurasian westerly jet¹⁷, and the observational decreased typhoon activity in the western North Pacific but increased hurricanes in the western Atlantic in the past four decades¹⁸.

SA and EA are both the major aerosol emission sources with a high aerosol burden. In the early 2000s, the aerosol optical depth

(AOD, 550 nm) in SA and EA remains very similar. However, since the early 2010s, an Asian aerosol dipole (AAD) pattern has emerged, characterized by a continuous rise of aerosols in SA and a concurrent decline in EA^{19,20} (Fig. 1a, b). The AA reduction in EA is primarily a consequence of the aggressive emission controls in China²¹. Consistently, the change of all-sky shortwave (SW) instantaneous radiative forcing (IRF) at the top-of-atmosphere (TOA) (see “Methods” section), where a negative trend means more reflection to space, displays a clear dipole pattern in Asia (Fig. 1c). It reflects the dominant role of changes in AAs in determining the SW IRF changes in this region. The SW IRF has a negative trend of $-0.91 \text{ W m}^{-2} \text{ decade}^{-1}$ from 2003 over SA, together with a positive trend of $1.23 \text{ W m}^{-2} \text{ decade}^{-1}$ from 2011 over EA (Fig. 1d).

Examination of how the regional AA changes influence the climate is not only of interest from a scientific standpoint but also has critical societal and economic repercussions because it directly affects the lives of Asian populations. Many studies have investigated the climate impacts of the increasing AOD in both SA and EA, representative of the change up to the early 2000s^{22–25}. However, little is known about the climate influences of the emerging AAD pattern that is anticipated to persist in the coming decades¹⁹. Further, the current Coupled Model Inter-comparison Project Phase 6 (CMIP6) models do not capture the observed AAD pattern in the recent decade largely due to the unrealistic emission dataset used²⁰, rendering it difficult to study the climate impacts using the existing climate model results.

Here idealized radiative perturbations are used to probe the climate impacts of the evolving AAs in Asia. Note that the observed AOD changes in SA and EA are both dominated by the

¹NOAA/Geophysical Fluid Dynamics Laboratory, Princeton, NJ, USA. ²Cooperative Programs for the Advancement of Earth System Science (CPAESS), University Corporation for Atmospheric Research, Boulder, CO, USA. ³Scripps Institution of Oceanography, University of California San Diego, La Jolla, CA 92093, USA. ⁴Department of Urban and Environmental Engineering, Ulsan National Institute of Science and Technology, Ulsan 44919, Republic of Korea. ⁵Max-Planck Institute for Meteorology, Hamburg, Germany. ⁶NASA Goddard Space Flight Center, Earth Sciences Division, Greenbelt, MD, USA. ⁷Goddard Earth Science Technology and Research II, University of Maryland, Baltimore County, Baltimore, MD, USA. [✉]email: baoqiang.xiang@noaa.gov

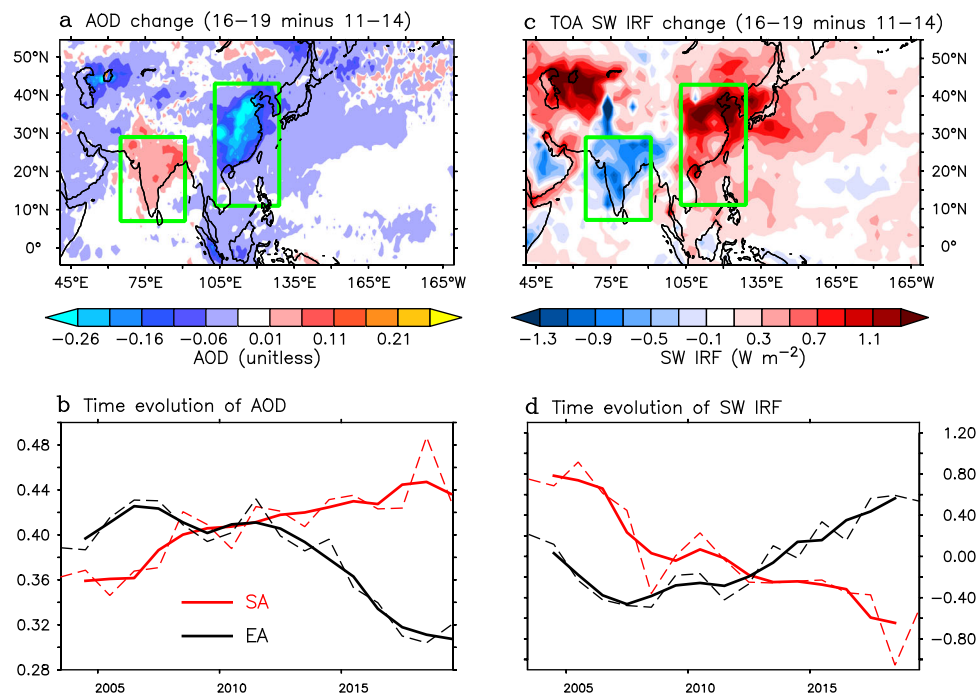


Fig. 1 Observed changes in aerosol optical depth (AOD) and shortwave instantaneous radiative forcing (SW IRF) at TOA since 2003. **a** Difference of AOD (550 nm) between the period 2016–19 and 2011–14 from a combined dataset of MODIS Terra and Aqua. **b** The time evolution of AOD over South Asia (SA) and East Asia (EA) averaged over the regions denoted by the green boxes in the upper panels from 2003 to 2019. Dashed (solid) lines denote the yearly mean (3-year running mean) results. **c, d** are similar to **(a)** and **(b)** but for the observed changes in all-sky SW IRF at TOA.

variation of nonabsorbing sulfate aerosols in the recent decade²⁶, consistent with the trends in SW IRF (Fig. 1c, d)²⁷. Given this, two coupled sensitivity experiments were performed by perturbing the solar constant over SA and EA to mimic the dominant impacts of the scattering aerosol changes using a state-of-the-art Geophysical Fluid Dynamics Laboratory (GFDL) climate model²⁸ (see “Methods” section and Supplementary Fig. 1). Each perturbed coupled experiment is an ensemble average of six realizations, which differ from one another in the initial conditions. For comparison, we also carried out Atmospheric Model Intercomparison Project (AMIP) simulations with the same atmospheric model component forced with fixed climatological sea surface temperature (SST) and sea ice concentration obtained from the coupled control simulation (see “Methods” section).

RESULTS

Annual mean climate changes

Figure 2 compares the annual mean climate responses to the same effective SW radiative forcing related to the SA aerosol increases and EA aerosol decreases (see “Method” section). The SA aerosol increases result in a weak global mean surface air temperature (SAT) cooling (-0.06°C), and the cooling pattern is rather homogenous in the tropics except for the strong SA cooling (Fig. 2a). The EA aerosol decreases yield a higher global mean SAT warming of 0.10°C . This is qualitatively consistent with other sensitivity experiments that the removal of AAs leads to a global mean temperature increase^{12,23,29}.

Obvious differences exist in terms of the land-sea contrast and interhemispheric contrast between these two cases (Fig. 2). For SA aerosol increases, the land has the same magnitude of cooling as the ocean, while for EA aerosol decreases, the land warming is about 2.6 times more intense than the ocean (0.18°C vs. 0.07°C). The increased land-sea thermal contrast may strengthen the global monsoon in the EA forcing case. The EA aerosol decreases

have a stronger interhemispheric asymmetry, characterized by 7.6 times stronger SAT warming in the northern hemisphere than the southern hemisphere (Fig. 2b). The EA forcing is also far-reaching, extending into the North Pacific and North Atlantic, and a large portion of North America and Europe (Fig. 2b). The warming in Europe mainly reflects the influence of a positive North Atlantic Oscillation (NAO) circulation pattern. The above results show that the interhemispheric climate response is sensitive to the geographic location in which the radiative perturbation occurs, with the forcing in the westerly wind regime exciting a more global climate response than that in the tropical monsoon regime.

We further investigated the changes in zonally averaged temperature and zonal winds. For the SA aerosol increases, the temperature response over the tropics is fairly symmetric about the equator although the maximum zonal-mean cooling takes place slightly north of the forcing region (Fig. 2c). In both hemispheres, the subtropical jet is decelerated together with a southward-shifted northern subtropical jet (Fig. 2c and Supplementary Fig. 2a). For the EA aerosol decreases, the zonal-mean temperature response exhibits prominent interhemispheric asymmetry with its peak on the northern edge of the forcing region (Fig. 2d). A dynamically coherent northward shift for the northern subtropical jet is observed, which extends to the near-surface (Fig. 2d and Supplementary Fig. 2b). The amplitude of the jet response is much stronger in the EA forcing than in the SA forcing.

For both cases, an anomalous cross-equatorial Hadley cell is excited (Fig. 2c, d). This is in agreement with many previous studies that an interhemispheric asymmetric energy perturbation could drive changes in atmospheric meridional circulations as well as the Intertropical Convergence Zone (ITCZ) location^{4,5,30,31}.

Combined annual mean climate impacts of AAD

What are the net climate consequences due to the recent AAD pattern? We infer the combined effects from the addition of the responses to SA and EA forcings assuming linearity. Considering

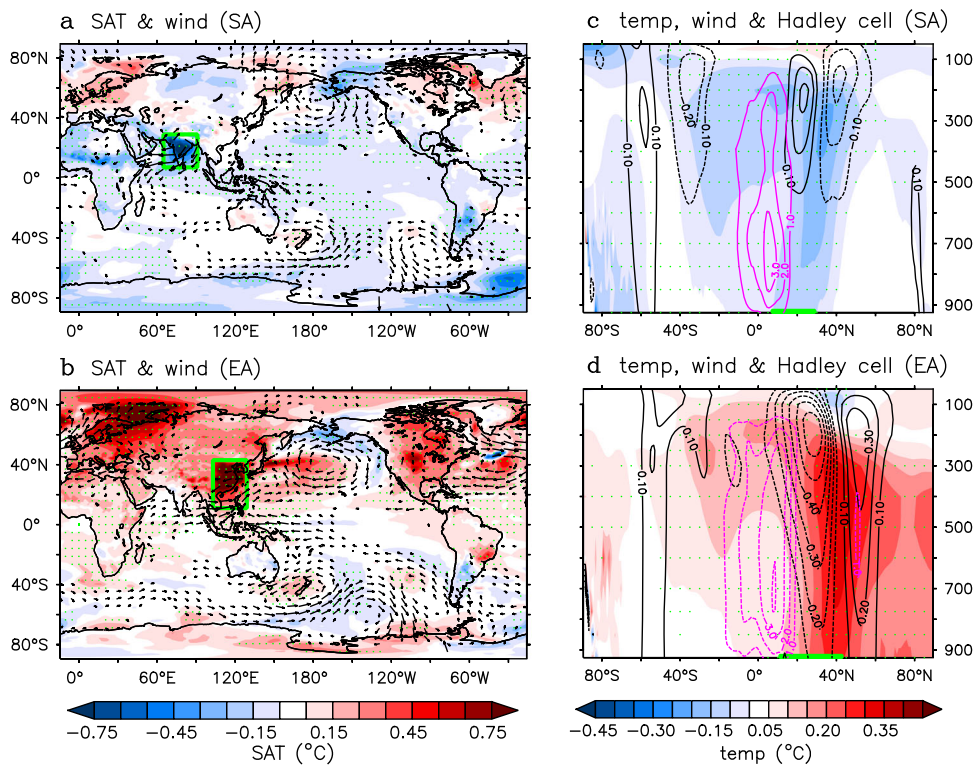


Fig. 2 Annual mean climate responses to the radiative forcings related to the SA aerosol increases and EA aerosol decreases. **a** Annual mean changes in surface air temperature (SAT, shading) and 850 hPa winds (vector in m s^{-1} , only showing the vectors when wind speed anomalies exceed 0.1 m s^{-1}) associated with the SA aerosol increases induced radiative forcing. **c** Annual mean changes in zonally averaged temperature (shading) and zonal winds (black contours in m s^{-1}). Purple contours represent the corresponding meridional mass flux changes (10^9 kg s^{-1}). Green lines at the bottom indicate the latitudes with the prescribed forcings. Green stippling indicates the regions with significant changes in SAT (left panels) and zonal mean temperature (right panels) at the 5% significance level. **b, d** are similar to (a) and (c) but for the results related to EA aerosol decreases.

the relative magnitude of the observed trend of aerosol-induced SW IRF and the imposed forcing between two domains (see “Methods” section), a scaled combination of these two experiments ($0.53^* \text{SA} + \text{EA}$) is shown here (Fig. 3a). Despite negligible net global radiative forcing (0.11 W m^{-2}) and small global mean SAT change, the AAD induces an evident poleward shift of the northern subtropical jet along with marked surface warming north of 30°N (Fig. 3a). The North Atlantic sector features a positive phase of NAO and the Scandinavian blocking, largely responsible for the pronounced warming in Europe (Fig. 3a). Remarkably, the combined effect on the North Pacific temperature is reminiscent of a significant negative phase Pacific Decadal Oscillation (PDO) (Fig. 3a), because the atmospheric circulation change over the North Pacific tends to reinforce each other for these two cases (Fig. 2a, b). Meanwhile, an intensified Walker circulation is observed in the equatorial Indo-western Pacific, contributing to a La Niña-like SST pattern (Fig. 3a). In the southern hemisphere, a prominent wave train pattern with cooling and warming patches extends from the south of Australia to the Weddell Sea in the southern hemisphere.

Isolation of the AAD-driven climate from observations is of challenge, partially because of the limited period of observations as well as the strong impacts of other external forcings and internal variability. Here we construct an index to represent the SAT difference between EA and SA (see “Methods” section), and find a similar temperature pattern in the historical period (1900–2015) (Fig. 3b). In particular, the surface warming is rather robust in Europe but the significant warming only occurs in a small region in North America. The upper-tropospheric circulation also exhibits a coherent pattern similar to the modeling results,

albeit the zonal mean component is stronger than in the model (Fig. 3b). Note that the wave-train pattern in the southern hemisphere is less pronounced in observations in comparison to the modeling results.

Further, the mean SAT change in the northern extratropics ($0^\circ\text{--}360^\circ\text{E}$, $30^\circ\text{--}90^\circ\text{N}$) has a magnitude of $0.24 \pm 0.10^\circ\text{C}$, while the SAT change in Europe ($10^\circ\text{W}\text{--}60^\circ\text{E}$, $40^\circ\text{--}75^\circ\text{N}$) is much larger ($0.47 \pm 0.09^\circ\text{C}$). By comparing the idealized forcing magnitude (Supplementary Fig. 1) and the observed SW IRF (see “Methods” section), we can quantify the recent AAD-induced annual mean warming rate for the northern extratropics beyond 30°N ($0.024 \pm 0.010^\circ\text{C decade}^{-1}$) and for Europe ($0.049 \pm 0.009^\circ\text{C decade}^{-1}$). For perspective, the total observed SAT trend over the full historical period (1900–2019) is $0.12^\circ\text{C decade}^{-1}$ for the northern extratropics and $0.13^\circ\text{C decade}^{-1}$ for Europe, which have mainly been driven by the increasing greenhouse gas concentrations.

It is concluded that the AAD-induced SAT change is prominent and significantly exacerbates the northern hemisphere warming acting upon the background greenhouse gases-induced warming effect, despite the largely localized and weak (a global mean of 0.11 W m^{-2}) forcing. Additionally, in observations, the local aerosol emission change in EA can influence the AOD and SW IRF forcing in the downstream western North Pacific through mean advection (Fig. 1a, c), potentially leading to more severe climate impacts than the estimation from the idealized localized forcing experiment presented here. The effects of the regional shift in aerosol emissions and the resultant spatial gradient of forcing should be taken into consideration when tackling climate change and the associated extremes in the future.

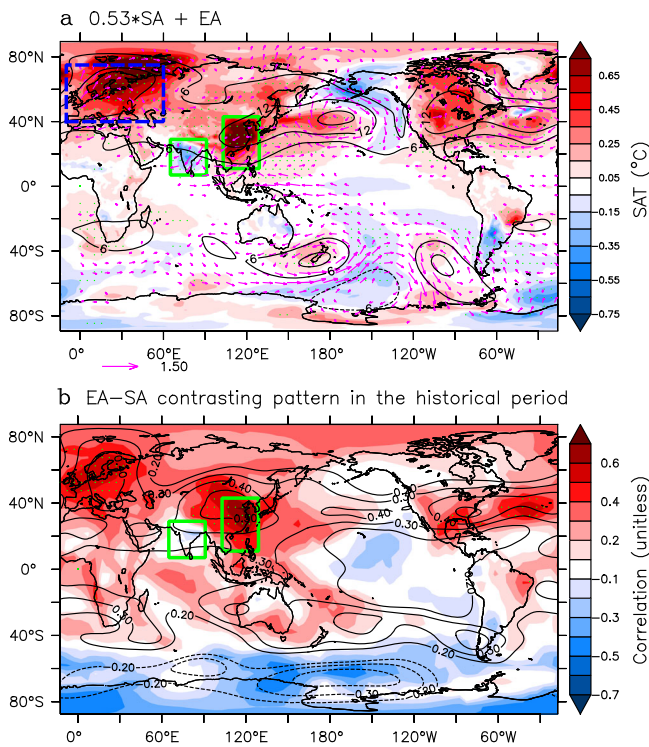


Fig. 3 Annual mean climate linked to the Asian aerosol dipole (AAD) pattern from model and observations. **a** Annual mean changes in SAT (shading), 850 hPa winds (vector in m s^{-1} , only showing the vectors when wind speed anomalies exceed 0.1 m s^{-1}), and H200 (contours in meter) associated with AAD measured by a scaled combination of two experiments ($0.53^*\text{SA} + \text{EA}$). Stippling denotes the regions with significant SAT change at the 5% significance level. The dashed box denotes the region of Europe. **b** The correlation coefficient between the observational SAT (shading), H200 (contours), and the observational SAT dipole index, which is defined by the 3-year running mean SAT contrast between EA and SA during 1900–2015 (see “Methods” section). Stippling denotes the regions with significant SAT correlation at the 5% significance level by considering the effective sample size.

Summertime climate response

The SA summer monsoon (also known as Indian Summer Monsoon) and EA summer monsoon regulate the seasonal march of precipitation and circulation in the Indo-western Pacific sector³². The change in monsoon rainfall affects ecosystems, industry, and agriculture, especially the food security of billions of people in Asia, and will potentially incur large societal costs. Extensive literature underlines the aerosol impacts on monsoon rainfall both in observations and numerical model simulations^{6,22,24,25,33–37}. Figure 4 shows the boreal summertime (June–August, JJA) climate response to the SA and EA aerosol changes. The SA aerosol increases result in considerably weakened SA summer monsoon with indigenous characteristics of suppressed rainfall and circulations (Fig. 4a). This lends support to the assertion that the increasing aerosols are responsible for the decreasing Indian monsoon rainfall since around the 1940s³⁵. The dramatically reduced rainfall is only evident over the Bay of Bengal and absent in the Arabian Sea, although the imposed forcing is of a similar magnitude in the two regions (Supplementary Fig. 1a). The north equatorial Indian Ocean receives prominently enhanced precipitation along with strong lower-tropospheric wind convergence (Fig. 4a). Strikingly, central Africa and Sahel experience significantly increased rainfall which can be explained via the so-called “Monsoon-Desert Mechanism” through the westward propagation of baroclinic Rossby waves³⁸.

The EA aerosol decreases force a cyclonic circulation in the lower troposphere and enhanced precipitation with the maximum located in the northern South China Sea, a signature of strengthened EA summer monsoon (Fig. 4b). This agrees with other studies that increased aerosol emissions in Asia suppress the Asian summer monsoon²⁴, while reduced aerosols from future projections tend to enhance summer monsoon precipitation³⁷. The strengthened monsoon flows are not just confined to the forcing region but extend westward from the South China Sea to the western Arabian Sea via the westward propagated baroclinic Rossby waves.

Compared to the EA aerosol decreases, the local land summertime SAT change for the SA aerosol increases is much weaker (Fig. 4d vs. 4e). This is physically coherent with the contrasting land precipitation changes (Fig. 4a, b). The SA forcing yields a 2.7 times stronger land precipitation response than the EA forcing ($-0.77 \text{ mm day}^{-1}$ vs. 0.29 mm day^{-1}). Consequently, a large SW radiative response related to cloud changes largely compensates for the imposed radiative cooling from the forcing (Supplementary Fig. 3), yielding a weak SAT change. The less vigorous local land precipitation response in the EA experiment is ascribed to, at least partially, the fact that a higher (lower) latitude forcing favors a rotational (divergent) wind response. As expected, the combined effect due to AAD features a dipole precipitation change pattern (Fig. 4c).

A baroclinic response over the local forcing regions is seen for both cases by comparing the lower and upper-tropospheric circulation changes (Fig. 4). Distinct from the SA aerosol increases case (Fig. 4d), the EA aerosol decreases have strong and far-reaching changes in SAT and 200 hPa geopotential height (H200) over the northern subtropics and mid-latitudes (Fig. 4e). The circulation is rather barotropic. The combined northern hemisphere effect due to AAD is largely dominated by the EA aerosol decreases (Fig. 4f). Why is the EA forcing more effective in driving the remote northern climate than the SA forcing? One possibility is that a large portion of the EA forcing is located in the westerly jet serving as a waveguide for circumglobal barotropic stationary waves, while the SA forcing is located in the tropics and induces westward propagating baroclinic Rossby wave responses (Fig. 4d, e)^{39,40}.

To test the above hypothesis, we carry out linear baroclinic model⁴¹ (LBM) experiments forced with a similar pattern to the precipitation changes over the forced domain and the surrounding regions (see “Methods” section). For the SA aerosol increases, the H200 anomaly shows a tropically confined and rather equatorially symmetric pattern (Fig. 5a). For the EA aerosol decreases, the atmospheric response is characterized by a westward propagating Rossby response (Fig. 5d). For both cases, the upper-tropospheric responses differ dramatically between the LBM results and the fully coupled model results, inferring that the local convective forcing solely cannot explain the global circulation changes observed in the coupled model simulations (Fig. 4d, e).

How to understand the above discrepancy between the fully coupled model and LBM results? This is tied to the contrasting air-sea feedback between these two cases. For the SA aerosol increases, the impacts of the enhanced convective heating over the equatorial Indian Ocean largely mirror those of the SA aerosol increases (Fig. 5b). Therefore, the combined effect of the local SA forcing and remote impacts from the equatorial Indian Ocean is weak and largely anchored in northern Africa and southern Eurasia (Fig. 5c), reasonably reproducing the fully coupled model results (Fig. 4d). For the EA aerosol decreases, the center of enhanced convection takes place in the northern South China Sea mainly to the south of the westerly jet (Fig. 4b, e), limiting its direct climate impacts. But, the downstream SST warming and the resultant diabatic heating over the western North Pacific are at the center of the westerly jet, facilitating a pronounced barotropic response toward North America (Fig. 5e). The combination of the local EA forcing and the downstream western North Pacific forcing

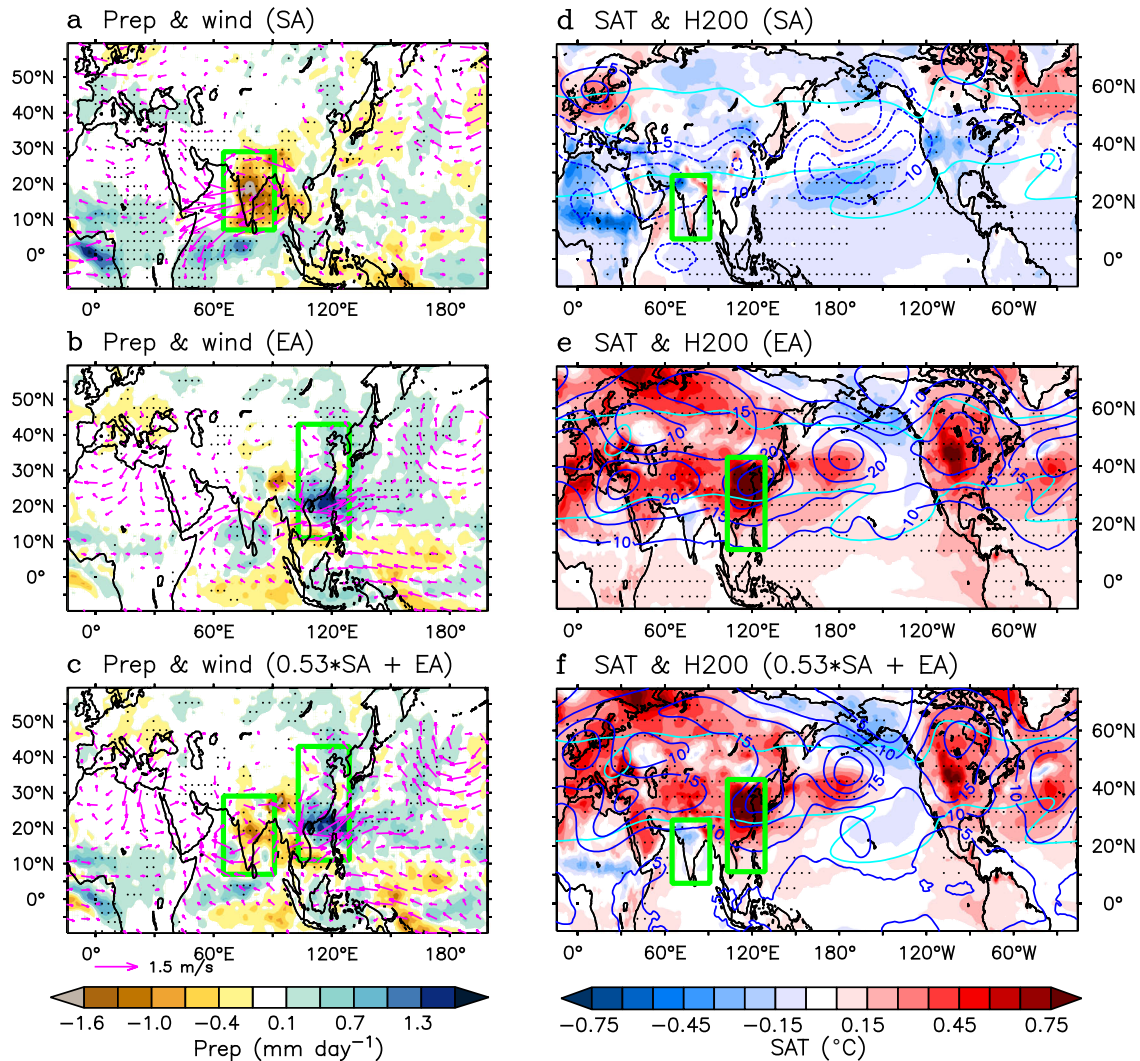


Fig. 4 Summertime climate responses to the recent Asian aerosol change-induced radiative forcings. Summertime (JJA) atmospheric precipitation (shading) and 850 hPa wind (vectors in m s^{-1} , only showing the vectors when wind speed anomalies exceed 0.1 m s^{-1}) responses to the SA aerosol increases induced radiative cooling (a), and EA aerosol decreases induced radiative heating (b). Similar to (a) and (b), c shows the AAD impacts measured by a scaled combination of two experiments ($0.53 \times \text{SA} + \text{EA}$). (d-f) are similar to (a-c) but for the corresponding summertime responses of SAT (shading) and 200 hPa geopotential height (H200, blue contours in meters). The cyan contours denote the 10 m s^{-1} climatological summertime 200 hPa zonal winds from the control simulation. The green boxes indicate the regions with the radiative perturbation. Stippling denotes the regions with significant precipitation (left panels) and SAT (right panels) changes at the 5% significance level.

shows a much stronger H200 response than that from the SA case (Fig. 5c vs. 5f), in agreement with the coupled model results (Fig. 4d vs. 4e). In sum, the northern hemisphere summertime climate driven by the SA forcing is substantially canceled by the convective changes over the equatorial Indian Ocean (Fig. 6a). By contrast, for the EA aerosol decreases, the air-sea coupling and the resultant downstream SST warming in the western North Pacific are crucial in amplifying and spreading the forcing effect to other regions in the northern hemisphere (Fig. 6b). This highlights the importance of the background state and air-sea feedback in regulating the climate responses to external forcings.

Then, what is responsible for the formation of SST warming in the western North Pacific for EA aerosol decreases? Firstly, it is related to the eastward warm temperature advection from the EA forcing region by the mean westerly jet. Secondly, as part of the extratropical stationary wave train, the anomalous North Pacific high (weakened Aleutian low) (Fig. 2b) tends to increase the downward SW radiation as well as excite westward propagated downwelling oceanic Rossby waves. The latter strengthens the

western boundary currents and oceanic warm advection. So, the SST warming in the western North Pacific is reinforced by ocean dynamics. Note that the weakened Aleutian low is also present in the AMIP simulation (forced with fixed SST and sea ice concentration, Supplementary Fig. 4a), indicating that the circulation anomalies in the North Pacific are largely due to the forcing itself rather than the feedback. In the Bering Sea and the Gulf of Alaska, weak cooling takes place where the wind-evaporation-SST feedback and oceanic cold advection come into play (Supplementary Fig. 4b).

DISCUSSION

Compared to the large hemispheric-scale shift of AAs around the 1980s, the emerging AAD represents a regional shift of AAs. The experiments here suggest that the climate response to the regional-scale AAD differs markedly from the hemispheric-scale shift of AAs around the 1980s reported in previous studies^{42–44}. Geographically, the imposed dipole forcing is both within the

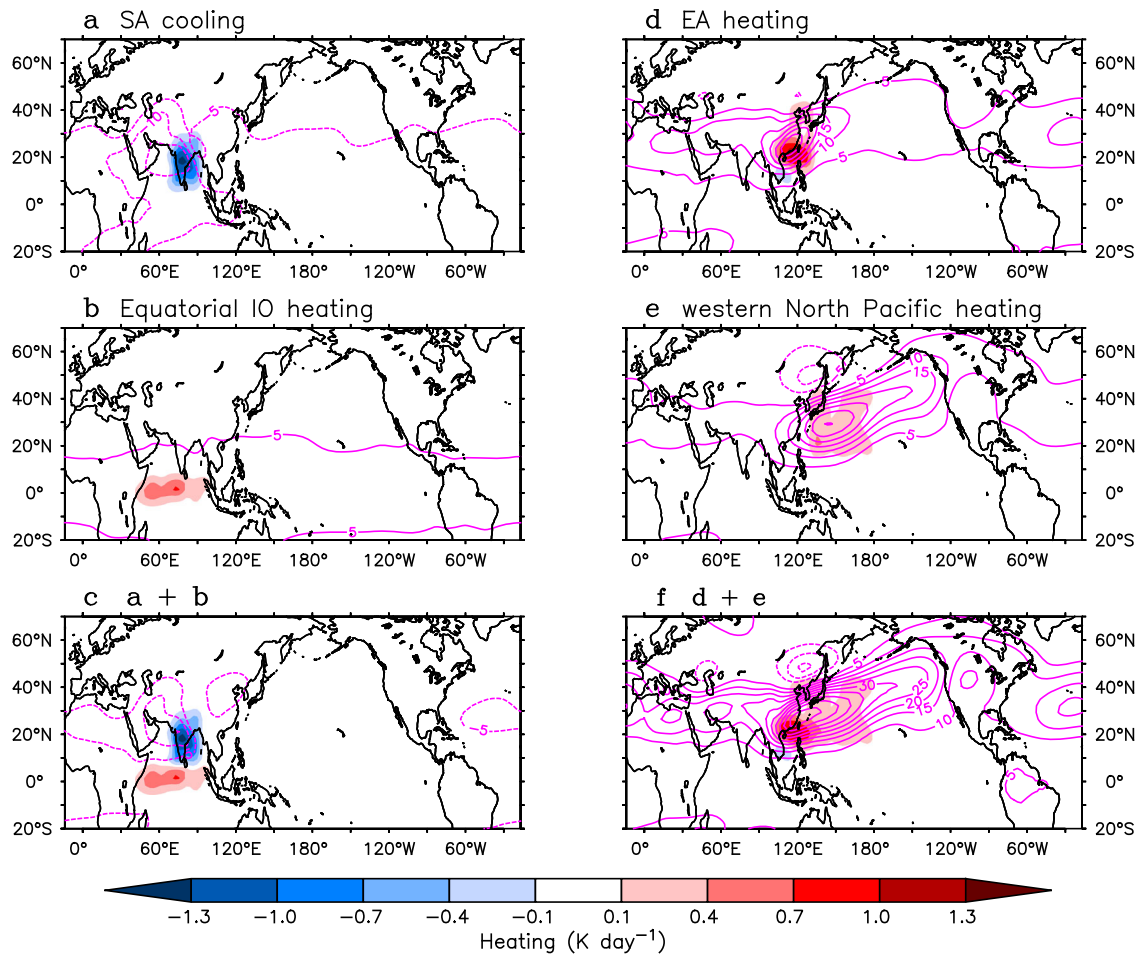


Fig. 5 Identification of critical regions responsible for the climate responses in the coupled model results using the LBM model. **a** Steady-state H2O responses (contours in meters) to the prescribed diabatic forcing in SA with the maximum at the mid-troposphere (shading) with the summertime background mean states. **b** similar to (a) but for the forcing over the equatorial Indian Ocean. **c** represents the sum of (a) and (b). The heating and cooling forcings are prescribed based on the precipitation pattern from Fig. 4a. **d–f** are similar to (a–c) but with the prescribed diabatic forcing derived from the precipitation pattern with EA aerosol decreases forcing (Fig. 4b).

monsoon regions and only about 4000 km apart between the opposing poles (Supplementary Fig. 1). The resultant maximum precipitation response is roughly at the same latitudes within the forcing domains (Fig. 4a vs. 4b). Nevertheless, the SA aerosol increases and EA aerosol decreases induce distinctive global impacts. The EA forcing has a strong fingerprint over the northern mid-latitudes with a prominent interhemispheric asymmetry of SAT. By contrast, the response of the SA forcing has its major loading over the tropical oceans with a rather equatorially symmetric pattern. The reasons behind the contrasting response are due to the distinct air-sea feedbacks as well as the distinct background mean states. Specifically, the westerly jet near EA advects the temperature anomalies and acts as a waveguide for marked circulation changes in the northern mid-latitudes. The results not only have important implications for decadal prediction but also have vital ramifications for understanding the climate change associated with AA variations in the historical period up to the early 2000s.

Note that the observational effective radiative forcing due to AAs has become a reduced negative globally since 2000, resulting in less aerosol-induced cooling effect⁴⁵. Further, the emerging AAD pattern since the early 2010s exacerbates the northern hemisphere warming, in particular over Europe. This study sheds light on the importance of the pattern effect of forcing in regulating the global climate. The magnitude of global SAT response to the regionally imposed forcings generally agrees with

previous studies^{46–48}, while the design of sensitivity experiments in this study (a relatively shorter integration but more ensembles in a fully coupled model) is more relevant to study the near-term or decadal timescale impacts due to the recent observational AAD. More importantly, we provide detailed physical interpretation to understand the distinct climate response to forcings in the tropical monsoon region vs. extratropical westerly regimes, and quantify the climate impacts due to the recent AAD based on the observed SW IRF.

In the boreal summer, the EA aerosol decreases induce a zonal wave number-5 pattern in addition to the zonal-mean increase in H2O (Fig. 4e), representing the so-called circumglobal teleconnection (CGT)⁴⁹. The CGT is one of the dominant modes in boreal summer extratropics and has a preferred phase position. Ding and Wang⁴⁹ suggested that the variation of SA summer monsoon can trigger the formation of the CGT, but our results support that the formation and intensity of CGT pattern are more susceptible to the EA aerosol decreases than the SA aerosol increases (Fig. 4d, e). Additionally, the land-atmosphere interaction may amplify this teleconnection pattern through soil moisture feedback⁵⁰.

The recent changes in aerosols may exacerbate the risks of extremes and their severity. Based on the summertime SAT response, increased AAs over India do not alleviate heat risks locally (Fig. 4d). In contrast, the reduction in EA AAs inadvertently increases the risk of heat extremes not only locally but also over North America and Europe^{16,51} (Fig. 4e). The AA reduction in EA

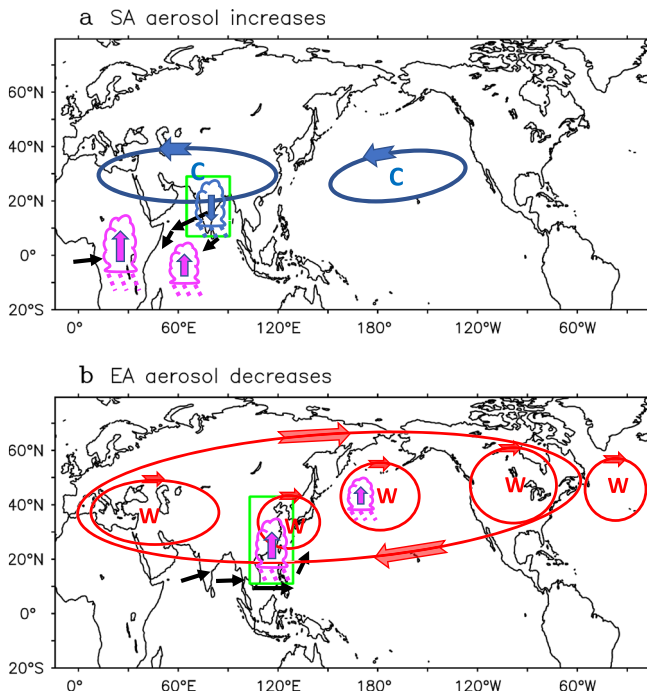


Fig. 6 A schematic diagram showing the summertime climate impacts due to the recent AAD. Convection, upper-tropospheric circulation and lower-tropospheric wind responses to the SA aerosol increases (a), and EA aerosol decreases (b). The upward and downward arrows indicate enhanced and suppressed convection, respectively. The black arrows represent the lower-tropospheric wind responses. The blue and red circles denote the upper-tropospheric responses. “C” and “W” represent surface cooling and warming, respectively.

may also exert severe impacts on the food production in distinct regions linked by the wave train pattern⁵². The wave train suppresses precipitation in Europe and central North America (Supplementary Fig. 5b), which may increase the risks of drought.

The regional pattern and magnitude of climate response to the aerosol perturbations show a salient model-dependency feature among this study and many previous studies^{39,46,47,51,53,54}. The reason behind this is complex, and is linked to the different model physics, experiment design, integration length as well as model mean state errors. A coordinated multi-model intercomparison project with the same forcing, such as the Regional Aerosol Model Intercomparison Project (RAMIP)⁵⁵, may help elucidate the physical processes controlling the regional pattern formation and understand the above model-dependent issue. This study explored the climate impacts of the change in the dominant scattering aerosols, while the change in absorbing aerosols, especially in SA, may also contribute to regulating the regional and global hydrological cycle and circulation response^{39,56,57}. The AAD-resultant indirect effect associated with the aerosol cloud interaction is another issue calling for further investigation.

METHODS

Observational and reanalysis data

We use a combined observed aerosol optical depth (AOD) dataset from Moderate Resolution Imaging Spectroradiometer (MODIS) Merged Dark Target and Deep Blue product on both the Terra and Aqua platforms⁵⁸. We also use the surface air temperature (SAT) dataset from UK Met Office HadCRUT5⁵⁹ and 200 hPa geopotential height from NOAA/CIRES/DOE 20th century reanalysis (V3)⁶⁰.

Estimation of instantaneous SW radiative forcing from observations

Following the method of previous work, we diagnose the observed shortwave instantaneous radiative forcing (SW IRF) as the difference between total, TOA SW radiative changes and the sum of individual SW radiative feedbacks diagnosed using the radiative kernel technique²⁷. The IRF is first estimated for clear-sky conditions, whereby the total SW radiative changes are diagnosed from the Clouds and Earth’s Radiative Energy System—Energy Balance and Filled Ed. 4.1 product (CERES-EBAF)⁶¹ and the SW water vapor and surface albedo feedbacks are diagnosed by multiplying radiative kernels derived from CloudSat/CALIPSO data⁶² by deseasonalized anomalies of specific humidity from version 7 Level 3 Atmospheric Infrared Sounder (AIRS) observations⁶³ and anomalies of surface albedo computed from CERES-EBAF surface fluxes⁶⁴, respectively. The estimated clear-sky SW IRF is then translated to an all-sky SW IRF by applying a cloud masking constant derived from aerosol double-call radiative transfer calculations from the Modern-Era Retrospective Analysis for Research and Applications, Version 2 (MERRA-2) reanalysis⁶⁵. Given data availability across these datasets, the SW IRF is diagnosed monthly since January 2003.

Throughout this work, positive anomalies and trends in the SW IRF correspond to more planetary SW absorption or less reflection to space. We note that the SW IRF only includes direct radiative effects and not indirect aerosol radiative effects or other rapid adjustments, which are included in the radiative feedback terms in the radiative kernel technique.

Observational global climate linked to the temperature contrast between EA and SA

We first remove the linear trend of the annual mean SAT and H200 from the historical period (1900–2015). A dipolar SAT index is built by subtracting the 3-year running mean SAT in SA from that in EA, and then performing a correlation analysis between this index and the 3-year running mean SAT and H200.

Climate model

We use a developmental version of the Geophysical Fluid Dynamics Laboratory (GFDL) next-generation atmospheric model version 4 (AM4)^{66,67}, as well as a fully coupled model using AM4 coupled with the ocean model used in GFDL Forecast-Oriented Low Ocean Resolution (FLOR) model⁶⁸. Both the atmospheric and oceanic models have an approximate 1° horizontal resolution. The external forcings, such as greenhouse gases and aerosols, are fixed at the year 2000 level. The model has been used for various radiative forcing experiments^{28,43,69,70}. One difference regarding the model configuration is that we turn off the interactive aerosols by prescribing the climatological aerosols estimated from a long control simulation to evaluate the direct aerosol climate effects. The model has realistic mean states, such as SST, winds, precipitation, and so on. Here we just show examples by comparing the observational and model-simulated annual mean precipitation and 200 hPa zonal winds (Supplementary Fig. 6), and annual mean SAT and net SW radiation at TOA (Supplementary Fig. 7).

We have conducted 150 years of control simulation as references. Two sensitivity experiments are performed by perturbing the solar constant to mimic the climate impacts of nonabsorbing aerosol radiative forcing changes. We impose the radiative forcing by proportionally perturbing the solar constant with the reference of the mean solar constant within the domain of EA (103°E–129°E, 11°N–43°N) and SA (65°E–91°E, 7°N–29°N), respectively. The design of these experiments is largely motivated by the observational AOD change pattern since the early 2010s (Fig. 1a)¹⁹, and the resultant forcing can be seen in Supplementary Fig. 1. Six ensembles are carried out with each integration for 50

years initialized at six different initial conditions from the control simulations. The analysis is based on the ensemble mean results during the last 30 years. A *t*-test is applied to test the difference between the sensitivity and the control simulation at the 5% significance level. Note that the global climate responses remain very similar between experiments with solar constant perturbation and with sulfate perturbation based on multi-model results participated in the Precipitation Driver and Response Model Intercomparison Project (PDRMIP)⁷¹. It further validates that the perturbation of solar constant can be a good proxy representing the change in nonabsorbing aerosols.

Similar to the coupled model experiments, we also conduct a corresponding AMIP-type simulation forced with the climatological SST and sea ice concentration from the control coupled model simulation. Each experiment is integrated for 50 years and the analyses are based on 50 years' mean. The imposed effective SW radiative forcing is estimated based on the AMIP-type simulation, which is nearly identical (0.11 PW) over these two domains considering the cloud radiative reflection from the AMIP control simulation. The domain averaged effective forcing is -16.4 Wm^{-1} and 11.9 Wm^{-1} in SA and EA, respectively. Note that the perturbed forcing magnitude is relatively about 10 (18) times stronger compared to the observed SW IRF over EA (SA) so as to isolate the prescribed external forcing effect to overlay the internal variability.

A scaled combination of SA aerosol increases and EA aerosol decreases and quantification of the SAT change due to the observed AAD

The observed SW IRF is -0.91 Wm^{-1} and $1.23 \text{ Wm}^{-1} \text{ decade}^{-1}$ over SA and EA, and the imposed radiative forcing is -16.4 Wm^{-1} and 11.9 Wm^{-1} in SA and EA, respectively. To match the observed contrast of SW IRF between SA and EA, we need to have a scaled combination of these two experiments: $0.53 \times \text{SA} + \text{EA}$.

To further compare with the observed temperature trend in the historical period, we need to further scale the SAT change by relating the ratio of the idealized forcing and the observed SW IRF in EA: $1.23/11.6 \times (0.53 \times \text{SA} + \text{EA})$, and the value is $0.024 \pm 0.010 \text{ }^{\circ}\text{C decade}^{-1}$ in the northern extratropics beyond 30°N and $0.049 \pm 0.009 \text{ }^{\circ}\text{C decade}^{-1}$ in Europe.

Linear baroclinic model (LBM)

To test the influences of convective heating on large-scale circulations, we carry out sensitivity experiments using the linear baroclinic model (LBM)⁴¹. The dry version of the LBM model consists of primitive equations linearized with a background basic state. Here we use the boreal summer (JJA) mean states as the background state. The model has a horizontal resolution of T42 and 20 vertical levels in σ coordinates. The heating pattern is based on the precipitation changes as shown in Fig. 4a, b. The vertical heating profile has a sinusoidal profile with its maximum at the level of around 500 hPa.

DATA AVAILABILITY

The MODIS Terra and Aqua data we use here are the monthly data which are available here: https://ladsweb.modaps.eosdis.nasa.gov/search/order/1/MOD08_M3-61,MYD08_M3-6. For the instantaneous radiative forcing estimates, the CERES data are available here: <https://ceres-tool.larc.nasa.gov/ord-tool/jsp/EBAF41Selection.jsp>, and the AIRS data are available here: <https://disc.gsfc.nasa.gov/datasets?page=1&source=AQUA%20AIRS&keywords=airs%20version%207>, and the MERRA-2 data are available here: <https://disc.gsfc.nasa.gov/datasets?project=MERRA-2>. The UK Met Office HadCRUT5 data can be obtained from <https://www.metoffice.gov.uk/hadobs/hadcrut5/The>. NOAA/CIRES/DOE 20th century reanalysis (V3) data are provided by the NOAA PSL, Boulder, Colorado, USA, from the website at <https://psl.noaa.gov>. The model results are available from the corresponding author upon request and with the permission of NOAA.

CODE AVAILABILITY

The data analysis code is available from the corresponding author upon request.

Received: 14 December 2022; Accepted: 13 June 2023;

Published online: 30 June 2023

REFERENCES

- Rosenfeld, D. Suppression of rain and snow by urban and industrial air pollution. *Science* **287**, 1793–1796 (2000).
- Xie, S.-P., Lu, B. & Xiang, B. Similar spatial patterns of climate responses to aerosol and greenhouse gas changes. *Nat. Geosci.* **6**, 828–832 (2013).
- Wang, H., Xie, S.-P., Tokinaga, H., Liu, Q. & Kosaka, Y. Detecting cross-equatorial wind change as a fingerprint of climate response to anthropogenic aerosol forcing. *Geophys. Res. Lett.* **43**, 3444–3450 (2016).
- Ming, Y. & Ramaswamy, V. Nonlinear climate and hydrological responses to aerosol effects. *J. Clim.* **22**, 1329–1339 (2009).
- Ramaswamy, V. & Chen, C. T. Linear additivity of climate response for combined albedo and greenhouse perturbations. *Geophys. Res. Lett.* **24**, 567–570 (1997).
- Li, Z. et al. Aerosol and monsoon climate interactions over Asia. *Rev. Geophys.* **54**, 866–929 (2016).
- Boucher, O. et al. in *Climate Change 2013: The Physical Science Basis. Contribution of Working Group I to the Fifth Assessment Report of the Intergovernmental Panel on Climate Change* (eds Stocker, T. F. et al.) (Cambridge University Press, 2013).
- IPCC. in *Climate Change 2021: The Physical Science Basis. Contribution of Working Group I to the Sixth Assessment Report of the Intergovernmental Panel on Climate Change* (eds Masson-Delmonte, V. et al.) (Cambridge University Press, 2021).
- Deser, C. et al. Isolating the evolving contributions of anthropogenic aerosols and greenhouse gases: a new CESM1 large ensemble community resource. *J. Clim.* **33**, 7835–7858 (2020).
- Lamarque, J. F. et al. Historical (1850–2000) gridded anthropogenic and biomass burning emissions of reactive gases and aerosols: methodology and application. *Atmos. Chem. Phys.* **10**, 7017–7039 (2010).
- Grainer, C. et al. Evolution of anthropogenic and biomass burning emissions of air pollutants at global and regional scales during the 1980–2010 period. *Clim. Change* **109**, 163 (2011).
- Samset, B. H. et al. Climate impacts from a removal of anthropogenic aerosol emissions. *Geophys. Res. Lett.* **45**, 1020–1029 (2018).
- Wang, Z., Lin, L., Yang, M. & Xu, Y. The effect of future reduction in aerosol emissions on climate extremes in China. *Clim. Dyn.* **47**, 2885–2899 (2016).
- Touma, D., Stevenson, S., Lehner, F. & Coats, S. Human-driven greenhouse gas and aerosol emissions cause distinct regional impacts on extreme fire weather. *Nat. Commun.* **12**, 212 (2021).
- Xu, Y., Lamarque, J.-F. & Sanderson, B. M. The importance of aerosol scenarios in projections of future heat extremes. *Clim. Change* **146**, 393–406 (2018).
- Luo, F. et al. Projected near-term changes of temperature extremes in Europe and China under different aerosol emissions. *Environ. Res. Lett.* **15**, 034013 (2020).
- Dong, B., Sutton, R. T., Shaffrey, L. & Harvey, B. Recent decadal weakening of the summer Eurasian westerly jet attributable to anthropogenic aerosol emissions. *Nat. Commun.* **13**, 1148 (2022).
- Murakami, H. Substantial global influence of anthropogenic aerosols on tropical cyclones over the past 40 years. *Sci. Adv.* **8**, eabn9493 (2022).
- Samset, B. H., Lund, M. T., Bollasina, M., Myhre, G. & Wilcox, L. Emerging Asian aerosol patterns. *Nat. Geosci.* **12**, 582–584 (2019).
- Ramachandran, S., Rupakheti, M. & Cherian, R. Insights into recent aerosol trends over Asia from observations and CMIP6 simulations. *Sci. Total Environ.* **807**, 150756 (2022).
- Zheng, B. et al. Trends in China's anthropogenic emissions since 2010 as the consequence of clean air actions. *Atmos. Chem. Phys.* **18**, 14095–14111 (2018).
- Dong, B., Wilcox, L. J., Highwood, E. J. & Sutton, R. T. Impacts of recent decadal changes in Asian aerosols on the East Asian summer monsoon: roles of aerosol-radiation and aerosol-cloud interactions. *Clim. Dyn.* **53**, 3235–3256 (2019).
- Merikanto, J. et al. How Asian aerosols impact regional surface temperatures across the globe. *Atmos. Chem. Phys.* **21**, 5865–5881 (2021).
- Liu, Y. et al. Anthropogenic aerosols cause recent pronounced weakening of Asian summer monsoon relative to last four centuries. *Geophys. Res. Lett.* **46**, 5469–5479 (2019).
- Song, F., Zhou, T. & Qian, Y. Responses of East Asian summer monsoon to natural and anthropogenic forcings in the 17 latest CMIP5 models. *Geophys. Res. Lett.* **41**, 596–603 (2014).
- Li, C. et al. India is overtaking China as the world's largest emitter of anthropogenic sulfur dioxide. *Sci. Rep.* **7**, 14304 (2017).

27. Kramer, R. J. et al. Observational evidence of increasing global radiative forcing. *Geophys. Res. Lett.* **48**, e2020GL091585 (2021).

28. Xiang, B., Zhao, M., Ming, Y., Yu, W. & Kang, S. M. Contrasting impacts of radiative forcing in the Southern Ocean versus Southern Tropics on ITCZ position and energy transport in one GFDL climate model. *J. Clim.* **31**, 5609–5628 (2018).

29. Levy, H. et al. The roles of aerosol direct and indirect effects in past and future climate change. *J. Geophys. Res. Atmos.* **118**, 4521–4532 (2013).

30. Kang, S. M., Held, I. M., Frierson, D. M. W. & Zhao, M. The response of the ITCZ to extratropical thermal forcing: idealized slab-ocean experiments with a GCM. *J. Clim.* **21**, 3521–3532 (2008).

31. Frierson, D. M. W. & Hwang, Y.-T. Extratropical influence on ITCZ shifts in slab ocean simulations of global warming. *J. Clim.* **25**, 720–733 (2012).

32. Wang, B. & Lin, H. O. Rainy season of the Asian–Pacific summer monsoon. *J. Clim.* **15**, 386–398 (2002).

33. Lau, K. M. & Kim, K. M. Observational relationships between aerosol and Asian monsoon rainfall, and circulation. *Geophys. Res. Lett.* **33**, L21810 (2006).

34. Menon, S., Hansen, J., Nazarenko, L. & Luo, Y. Climate effects of black carbon aerosols in China and India. *Science* **297**, 2250–2253 (2002).

35. Bollasina Massimo, A., Ming, Y. & Ramaswamy, V. Anthropogenic aerosols and the weakening of the South Asian summer monsoon. *Science* **334**, 502–505 (2011).

36. Wang, T. et al. Anthropogenic agent implicated as a prime driver of shift in precipitation in eastern China in the late 1970s. *Atmos. Chem. Phys.* **13**, 12433–12450 (2013).

37. Wilcox, L. J. et al. Accelerated increases in global and Asian summer monsoon precipitation from future aerosol reductions. *Atmos. Chem. Phys.* **20**, 11955–11977 (2020).

38. Rodwell, M. J. & Hoskins, B. J. Monsoons and the dynamics of deserts. *Q. J. R. Meteorol. Soc.* **122**, 1385–1404 (1996).

39. Dow, W. J., Maycock, A. C., Lofverstrom, M. & Smith, C. J. The effect of anthropogenic aerosols on the aleutian low. *J. Clim.* **34**, 1725–1741 (2021).

40. Wilcox, L. J. et al. Mechanisms for a remote response to Asian anthropogenic aerosol in boreal winter. *Atmos. Chem. Phys.* **19**, 9081–9095 (2019).

41. Watanabe, M. & Kimoto, M. Atmosphere–ocean thermal coupling in the North Atlantic: a positive feedback. *Q. J. R. Meteorol. Soc.* **126**, 3343–3369 (2000).

42. Wang, H. & Wen, Y.-J. Climate response to the spatial and temporal evolutions of anthropogenic aerosol forcing. *Clim. Dyn.* **59**, 1579–1595 (2021).

43. Kang, S. M., Xie, S.-P., Deser, C. & Xiang, B. Zonal mean and shift modes of historical climate response to evolving aerosol distribution. *Sci. Bull.* **66**, 2405–2411 (2021).

44. Fiedler, S. & Putrasahan, D. How does the North Atlantic SST pattern respond to anthropogenic aerosols in the 1970s and 2000s? *Geophys. Res. Lett.* **48**, e2020GL092142 (2021).

45. Quaas, J. et al. Robust evidence for reversal of the trend in aerosol effective climate forcing. *Atmos. Chem. Phys.* **22**, 12221–12239 (2022).

46. Persad, G. G. & Caldeira, K. Divergent global-scale temperature effects from identical aerosols emitted in different regions. *Nat. Commun.* **9**, 3289 (2018).

47. Kasoar, M., Shawki, D. & Voulgarakis, A. Similar spatial patterns of global climate response to aerosols from different regions. *npj Clim. Atmos. Sci.* **1**, 12 (2018).

48. Shindell, D. & Faluvegi, G. Climate response to regional radiative forcing during the twentieth century. *Nat. Geosci.* **2**, 294–300 (2009).

49. Ding, Q. & Wang, B. Circumglobal teleconnection in the northern hemisphere summer. *J. Clim.* **18**, 3483–3505 (2005).

50. Thompson, V. et al. The 2021 western North America heat wave among the most extreme events ever recorded globally. *Sci. Adv.* **8**, eabm6860 (2022).

51. Westervelt, D. M. et al. Local and remote mean and extreme temperature response to regional aerosol emissions reductions. *Atmos. Chem. Phys.* **20**, 3009–3027 (2020).

52. Kornhuber, K. et al. Amplified Rossby waves enhance risk of concurrent heat-waves in major breadbasket regions. *Nat. Clim. Change* **10**, 48–53 (2020).

53. Lewinschal, A. et al. Local and remote temperature response of regional SO₂ emissions. *Atmos. Chem. Phys.* **19**, 2385–2403 (2019).

54. Liu, L. et al. A PDRMIP multimodel study on the impacts of regional aerosol forcings on global and regional precipitation. *J. Clim.* **31**, 4429–4447 (2018).

55. Wilcox, L. J. et al. The regional aerosol model intercomparison project (RAMIP). *Geosci. Model Dev. Discuss.* **2022**, 1–40 (2022).

56. McCoy, I. L., Vogt, M. A. & Wood, R. Absorbing aerosol choices influences precipitation changes across future scenarios. *Geophys. Res. Lett.* **49**, e2022GL097717 (2022).

57. Samset, B. H. Aerosol absorption has an underappreciated role in historical precipitation change. *Commun. Earth Environ.* **3**, 242 (2022).

58. Sayer, A. M. et al. MODIS collection 6 aerosol products: comparison between Aqua’s e-Deep Blue, Dark Target, and “merged” data sets, and usage recommendations. *J. Geophys. Res. Atmos.* **119**, 13965–13989 (2014).

59. Morice, C. P. et al. An updated assessment of near-surface temperature change from 1850: the HadCRUT5 Data Set. *J. Geophys. Res. Atmos.* **126**, e2019JD032361 (2021).

60. Slivinski, L. C. et al. Towards a more reliable historical reanalysis: improvements for version 3 of the Twentieth Century Reanalysis system. *Q. J. R. Meteorol. Soc.* **145**, 2876–2908 (2019).

61. Loeb, N. G. et al. Toward a consistent definition between satellite and model clear-sky radiative fluxes. *J. Clim.* **33**, 61–75 (2020).

62. Kramer, R. J., Matus, A. V., Soden, B. J. & L’Ecuyer, T. S. Observation-based radiative kernels from CloudSat/CALIPSO. *J. Geophys. Res. Atmos.* **124**, 5431–5444 (2019).

63. Aumann, H. H. et al. AIRS/AMSU/HSB on the Aqua mission: design, science objectives, data products, and processing systems. *IEEE Trans. Geosci. Remote Sens.* **41**, 253–264 (2003).

64. Kato, S. et al. Surface irradiances of edition 4.0 Clouds and the Earth’s Radiant Energy System (CERES) energy balanced and filled (EBAF) data product. *J. Clim.* **31**, 4501–4527 (2018).

65. Gelaro, R. et al. The modern-era retrospective analysis for research and applications, version 2 (MERRA-2). *J. Clim.* **30**, 5419–5454 (2017).

66. Zhao, M. et al. The GFDL global atmosphere and land model AM4.0/LM4.0: 1. Simulation characteristics with prescribed SSTs. *J. Adv. Model. Earth Syst.* **10**, 691–734 (2018).

67. Zhao, M. et al. The GFDL global atmosphere and land model AM4.0/LM4.0: 2. Model description, sensitivity studies, and tuning strategies. *J. Adv. Model. Earth Syst.* **10**, 735–769 (2018).

68. Vecchi, G. A. et al. On the seasonal forecasting of regional tropical cyclone activity. *J. Clim.* **27**, 7994–8016 (2014).

69. Kang, S. M. et al. Extratropical–tropical interaction model intercomparison project (Etim-Mip): protocol and initial results. *Bull. Am. Meteorol. Soc.* **100**, 2589–2606 (2019).

70. Kang, S. M. et al. Walker circulation response to extratropical radiative forcing. *Sci. Adv.* **6**, eabd3021 (2020).

71. Samset, B. H. et al. Fast and slow precipitation responses to individual climate forcers: a PDRMIP multimodel study. *Geophys. Res. Lett.* **43**, 2782–2791 (2016).

ACKNOWLEDGEMENTS

We thank the review comments from Drs. Isaac M. Held, V. Ramaswamy, Qinghua Ding, and Wenhao Dong. Support for the Twentieth Century Reanalysis Project version 3 dataset is provided by the U.S. Department of Energy, Office of Science Biological and Environmental Research (BER), by the National Oceanic and Atmospheric Administration Climate Program Office, and by the NOAA Earth System Research Laboratory Physical Sciences Laboratory. S.P.X. was supported by NSF (AGS 1934392). S.M.K. was supported by the Research Program for the carbon cycle between oceans, land, and atmosphere of the National Research Foundation (NRF) funded by the Ministry of Science and ICT (NRF-2022M3I6A1090965). R.J.K. was supported by NASA award no. 80NSSC21K1968. This research from the Geophysical Fluid Dynamics Laboratory is supported by NOAA’s Science Collaboration Program and administered by UCAR’s Cooperative Programs for the Advancement of Earth System Science (CPAES) under award#NA21OAR4310383.

AUTHOR CONTRIBUTIONS

B.X. and S.-P.X. conceived of the research. B.X. performed model runs, analyzed the model results, and generated figures. R.J.K. analyzed the MODIS data and calculated the observed shortwave instantaneous radiative forcing. B.X. wrote the first draft and co-authors contributed to improving the analysis and interpolation.

COMPETING INTERESTS

The authors declare no competing interests.

ADDITIONAL INFORMATION

Supplementary information The online version contains supplementary material available at <https://doi.org/10.1038/s41612-023-00400-8>.

Correspondence and requests for materials should be addressed to Baoqiang Xiang.

Reprints and permission information is available at <http://www.nature.com/reprints>

Publisher’s note Springer Nature remains neutral with regard to jurisdictional claims in published maps and institutional affiliations.



Open Access This article is licensed under a Creative Commons Attribution 4.0 International License, which permits use, sharing, adaptation, distribution and reproduction in any medium or format, as long as you give appropriate credit to the original author(s) and the source, provide a link to the Creative Commons license, and indicate if changes were made. The images or other third party material in this article are included in the article's Creative Commons license, unless indicated otherwise in a credit line to the material. If material is not included in the article's Creative Commons license and your intended use is not permitted by statutory regulation or exceeds the permitted use, you will need to obtain permission directly from the copyright holder. To view a copy of this license, visit <http://creativecommons.org/licenses/by/4.0/>.

© The Author(s) 2023, corrected publication 2023